

Dressed four-wave mixing second-order Talbot effect

Haixia Chen, Xun Zhang, Dayu Zhu, Chang Yang, Tao Jiang, Huaibin Zheng, and Yanpeng Zhang*

Key Laboratory for Physical Electronics and Devices of the Ministry of Education & Shaanxi Key Lab of Information Photonic Technique, Xi'an Jiaotong University, Xi'an 710049, China

(Received 16 July 2014; published 21 October 2014)

We theoretically demonstrate second-order Talbot effect (SOTE) based on entangled photon pairs. The photon pairs are generated from the spontaneous parametric four-wave mixing (SPFWM) process in a cold atomic medium and can be taken as the imaging light in order to realize coincidence recording. A strong standing wave is used to create the electromagnetically induced grating in the entangled photon pairs channels. By changing the frequency detuning of the standing wave or the other optical fields participating in the process, we can manipulate the contrast of the second-order Talbot image. We use the second-order correlation function and the dressed-state picture to explain the SOTE occurring in the SPFWM process. Moreover, we demonstrate the scheme for SOTE based on the spatially correlated twin beams generated from the SPFWM process with injection. This scheme provides a convenient detection proposal for the SOTE at the cost of the image contrast. Compared to the previous self-imaging schemes, the present schemes have the characteristic of controllable image contrast and of nonlocal imaging, and thus, they might broaden their applications in imaging techniques and find applications in quantum lithography.

DOI: [10.1103/PhysRevA.90.043846](https://doi.org/10.1103/PhysRevA.90.043846)

PACS number(s): 42.50.Ct, 42.30.Va, 42.50.Gy, 42.50.St

I. INTRODUCTION

The Talbot effect is a near-field diffraction phenomenon first discovered by Talbot in 1836 [1]. When a plane wave transmits through a periodic structure, the image of the periodic structure is repeated at regular distances (called Talbot lengths) without need of any lens. Lord Rayleigh first analytically explained this physical phenomenon in 1881 [2]. He elucidated that the Talbot effect was a natural consequence of Fresnel diffraction and the Talbot length is $Z_T = 2a^2/\lambda$, in which a and λ are the period of the diffraction grating and the wavelength of the incident light beam, respectively. Over the past years, researchers have expanded this phenomenon into other areas such as waveguide arrays [3,4], surface waves [5,6], and atomic waves [7,8]. Interestingly, Talbot effects of second-harmonic generation [9,10] and two-wave mixings [11] extend this subject to nonlinear optics. We are aware that rogue waves can also form a nonlinear Talbot effect according to the cubic nonlinear Schrödinger equation [12]. It is worth mentioning that all the above investigations focus on the classical first-order Talbot imaging, which happens when a periodic object is illuminated with coherent light. Recently, second-order Talbot effect (SOTE) created by pseudothermal light has been observed experimentally [13,14]. The conditional Talbot effect and the second-order quantum Talbot effect with entangled photon pairs have been also theoretically discussed [15–17] and experimentally observed [18]. The quantum self-imaging may have extensive applications in quantum lithography [19,20], because of a possible breakthrough in lithographic resolution due to overcoming the diffraction limit. Furthermore, the electromagnetically induced first-order Talbot effect in atomic medium [21] was theoretically proposed for imaging ultracold atoms and molecules, where electromagnetically induced grating (EIG) was used to modify the optical response of the medium to the weak probe field. The first-order Talbot

effect with multiwave mixing (MWM) signals has been also proposed [22], where the atomic coherence resulted from the dressing field being used to control the nonlinear optical coefficient $\chi^{(3)}$ of the MWM signal [23,24]. A more thorough introduction on the Talbot effect can be found in Ref. [25] and references therein.

In this paper, we investigate the SOTE with the spontaneous parametric four-wave mixing (SPFWM) process in a cold atomic medium, where a strong standing wave is used to modulate the nonlinear optical coefficient $\chi^{(3)}$ of the SPFWM process periodically. Self-images of the induced EIG by the standing wave are formed from second-order correlation function. Especially, we use the frequency detunings of the optical fields to change the interference pattern of the EIG and thus control the Talbot effect. The dressed-state picture and the second-order correlation function are used in our analyses. Compared with previous studies [15,21], the advantages of our research include that a real grating object is avoided, the grating structure is much easier to be controlled, and higher-nonlinear processes are used. Moreover, we initially investigate SOTE via the spatially correlated twin beams when the SPFWM process is seeded with the phase-conjugate FWM and six-wave mixing (SWM) signals. The results show that the contrast of the second-order Talbot images obtained by the biphotonic correlation is superior to that obtained by the spatially correlated twin beams. However, the SOTE with the twin beams can be detected more easily due to the higher intensities of the twin beams.

This paper is organized as follows: In Sec. II, we use the dressed-state picture to explain the effect resulting from the standing wave in the SPFWM process. The formation of the EIG in the atomic medium is discussed and how to control the EIG is investigated; in Sec. III, we investigate the SOTE achieved by biphotonic correlation in the low-parametric-gain case and discuss the contrast control of the second-order Talbot imaging. The dressed-state picture and the second-order correlation function are applied to our analyses; in Sec. IV, we investigate Talbot effect in the high-parametric-gain case by

*Corresponding author: ypzhang@mail.xjtu.edu.cn

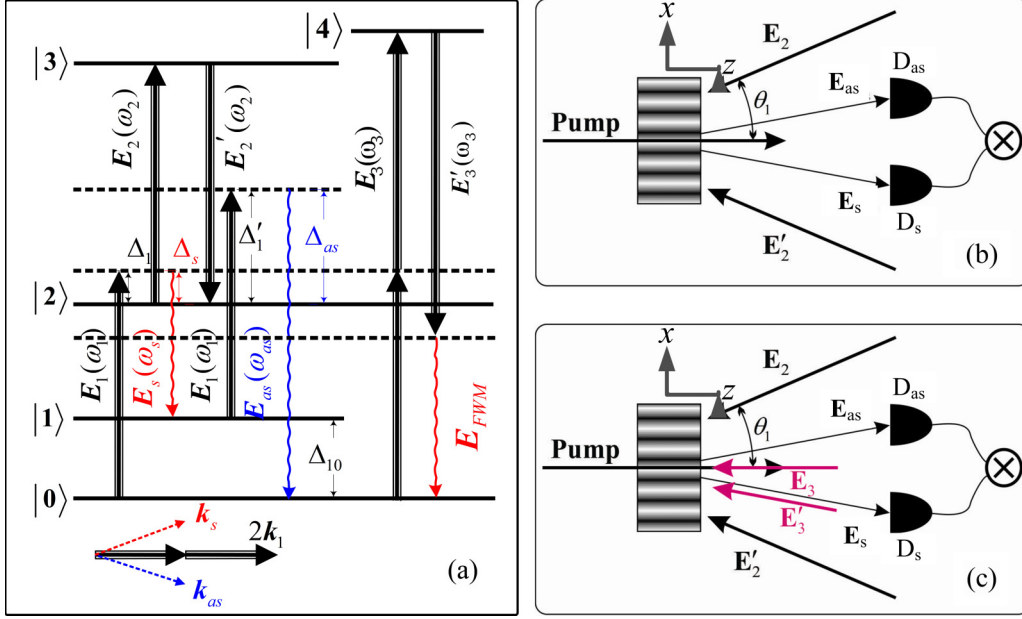


FIG. 1. (Color online) (a) A simplified atomic energy level diagram and the laser coupling configuration. The frequency difference between E_3 and E'_3 beam is equal to the ground-state splitting of the atomic system. (b) Schematic for SOTE achieved by the SPFWM process. (c) Schematic for SOTE achieved by the spatially correlated twin beams.

using the spatially correlated twin beams, when the SPFWM process is seeded with the phase-conjugate multiwave mixing signals; in the last section, we conclude this paper.

II. FORMATION OF EIG

At first, we introduce the SPFWM process for generating the entangled Stokes and anti-Stokes photons. Consider a cold atomic medium initially populated in the ground state $|1\rangle$ as shown in Fig. 1(a), in which $|0\rangle$ and $|1\rangle$ are two ground (hyperfine) states, and $|2\rangle, |3\rangle$, and $|4\rangle$ are three excited states. The $|0\rangle \rightarrow |2\rangle$ transition is pumped by the E_1 beam (with frequency ω_1 , frequency detuning Δ_1 , and wave vector \mathbf{k}_1). The $|2\rangle \rightarrow |3\rangle$ transition is coupled by the E_2 (with ω_2, Δ_2 , and \mathbf{k}_2) and E'_2 (with ω_2, Δ_2 , and \mathbf{k}'_2) beams. The $|2\rangle \rightarrow |4\rangle$ transition is coupled by E_3 (with ω_3, Δ_3 , and \mathbf{k}_3) and E'_3 (with ω_3, Δ_3 , and \mathbf{k}'_3) beams. The atomic resonant frequency for $|i\rangle \rightarrow |j\rangle$ transition is denoted as Ω_{ji} . The frequency detuning for each field is defined as resonant frequency minus optical field frequency. When only E_1 with strong intensity is on, an entangled source, denoted as Stokes signal E_s and anti-Stokes signal E_{as} , can be generated from the SPFWM process. The two entangled fields, satisfying the phase matching condition (PMC) $\mathbf{k}_s = 2\mathbf{k}_1 - \mathbf{k}_{as}$, propagate along two different directions as shown by the bottom panel in Fig. 1(a). According to the Liouville pathways [23,24], the density-matrix element $\rho_{21(s)}^{(3)}$ for the generated E_s field can be written as $\rho_{21(s)}^{(3)} = -iG_{as}^*G_1^2/(d'_{21}d'_{10}d_{21})$ via $\rho_{11}^{(0)} \xrightarrow{\omega_1} \rho_{21}^{(1)} \xrightarrow{\omega_{as}} \rho_{01}^{(2)} \xrightarrow{\omega_1} \rho_{21(s)}^{(3)}$, and $\rho_{20(as)}^{(3)}$ for the E_{as} field can be given as $\rho_{20(as)}^{(3)} = -iG_s^*G_1^2/(d_{20}d_{10}d'_{20})$ via $\rho_{00}^{(0)} \xrightarrow{\omega_1} \rho_{20}^{(1)} \xrightarrow{\omega_s} \rho_{10}^{(2)} \xrightarrow{\omega_1} \rho_{20(as)}^{(3)}$, where $d'_{21} = \Gamma_{21} + i\Delta'_1$, $d'_{10} = \Gamma_{10} + i(\Delta'_1 - \Delta_{as})$, $d_{21} = \Gamma_{21} + i(\Delta'_1 + \Delta_1 - \Delta_{as})$, $d_{20} = \Gamma_{20} + i\Delta_1$, $d_{10} = \Gamma_{20} + i(\Delta_1 - \Delta_s)$, and $d'_{20} = \Gamma_{20} + i(\Delta'_1 + \Delta_1 - \Delta_s)$ with

Δ_s and Δ_{as} representing the frequency detunings of the E_s and E_{as} signals, respectively. Δ'_1 is the frequency detuning of the E_1 field from the transition $|1\rangle \rightarrow |2\rangle$. The term $G_i = \mu_i E_i / \hbar$ ($i = 1, 2, 3$) is the Rabi frequency of the field E_i . The term Γ_{ij} is the decay rate between the energy levels $|i\rangle$ and $|j\rangle$.

Next, we consider the effect from the standing wave in the SPFWM process. The strong E_2 and E'_2 beams are open and propagate almost along the opposite direction of the E_1 beam as shown in Fig. 1(b). Each of them has a θ_1 angle with the E_1 beam. The E_2 and E'_2 beams interfere with each other to create a periodic standing wave in the transverse direction of the atomic medium. The x and z directions are set as shown in Fig. 1(b). Then the Rabi frequency of the standing wave can be written as $|G_{2r}(x)|^2 = G_2'^2 + G_2^2 + 2G_2G_2' \cos[2(k_2 \sin \theta_1)x]$ with the wave-vector module of the E_2 and E'_2 fields $k_2 = 2\pi/\lambda_2$. For a dressed-state analysis [26], state $|2\rangle$ and $|3\rangle$ plus the standing wave can be considered as a coupled atom-field system. The dressed states for this system can be given as $|G_{2r}(x)\pm\rangle$. Then the single Liouville pathway for the E_{as} signal will be changed into a double pathway: $\rho_{00}^{(0)} \xrightarrow{\omega_1} \rho_{G_{2r}(x)\pm 0}^{(1)} \xrightarrow{\omega_s} \rho_{10}^{(2)} \xrightarrow{\omega_1} \rho_{G_{2r}(x)\pm 0(as)}^{(3)}$. The corresponding density matrix element for the E_{as} signal is modified as $\rho_{20(as)}^{(3)} = -iG_s^*G_1^2/\{[d_{20} + |G_{2r}(x)|^2/d_{30}]d_{10}d'_{20}\}$ with $d_{30} = \Gamma_{30} + i(\Delta_1 + \Delta_2)$. We can find that the $\rho_{20(as)}^{(3)}$ varies periodically along the x direction due to the term $|G_{2r}(x)|^2$ and the period is $a_x = \lambda_2/(2\sin\theta_1)$. The periodical modulation of the $\rho_{20(as)}^{(3)}$ corresponds to the modulation of the nonlinear optical susceptibility $\chi^{(3)}$ of the SPFWM process, which can create an electromagnetically induced grating in the anti-Stokes channel. Self-images of such a nonmaterial grating can be obtained by second-order correlation function due to the spatial correlation of the anti-Stokes and Stokes signals. The dressing effect of the standing wave to the E_s signal can

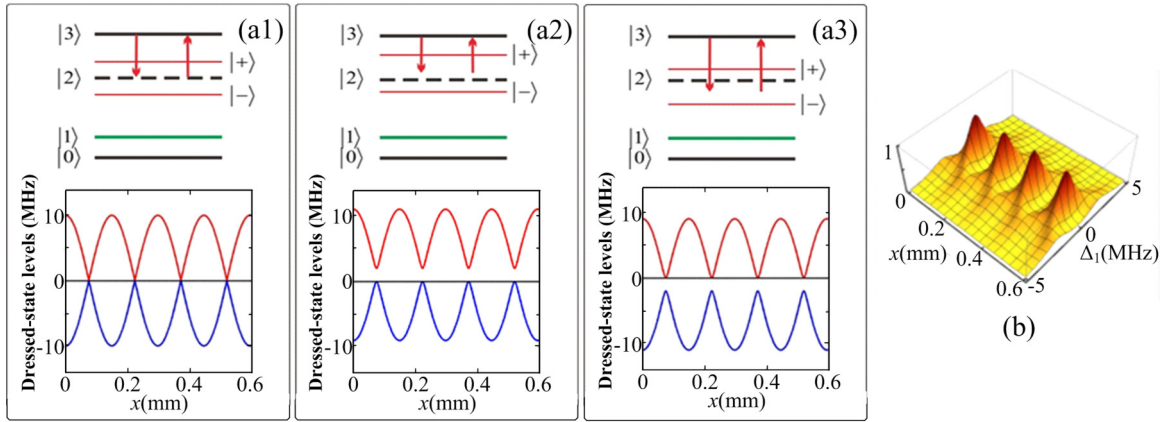


FIG. 2. (Color online) (a1)–(a3) Coupled atom-field systems (top panels) and dressed-state levels (bottom panels) with $\Delta_2 = 0, 2$, and -2 MHz, respectively. Other parameters are $G_2 = G'_2 = 5$ MHz and $a_x = 150 \mu\text{m}$. (b) Theoretical simulation of the normalized intensity distribution of the anti-Stokes signal versus x and Δ_1 at $z = 0$. Other parameters are $G_1 = 3.5$ MHz, $G_2 = G'_2 = 5$ MHz, $\Delta_2 = 0$, $\Gamma_{10} = 0.2\Gamma_{20}$, $\Gamma_{30} = 0.1\Gamma_{20}$, $\Gamma_{20} = \Gamma_{21} = 2\pi \times 6$ MHz, and $a_x = 150 \mu\text{m}$.

be analyzed in the same way, and we do not describe it any longer.

Now, we proceed to investigate the method for controlling the EIG. Using the dressed-state analysis, the eigenfrequencies corresponding to the dressed states $|G_{2f}(x)\pm\rangle$ can be calculated as $\lambda_{G_{2f}(x)\pm} = \Delta_2/2 \pm \sqrt{\Delta_2^2/4 + |G_{2f}(x)|^2}$. According to the eigenfrequencies expression $\lambda_{G_{2f}(x)\pm} = \pm|G_{2f}(x)|$ with $\Delta_2 = 0$, we show the dressed-state levels in the bottom panel of Fig. 2(a1), where the top panel shows the coupled atom-field system. We find that the two dressed states are symmetrical about state $|2\rangle$ and vary periodically along the x direction. The separation between the two dressed states is proportional to the Rabi frequency of the standing wave, so we can control the modulation amplitude of EIG by the intensities of the \mathbf{E}_2 and \mathbf{E}'_2 beams. We also show the dressed-state levels with Δ_2 taken as 2 and -2 MHz in Figs. 2(a2) and 2(a3), respectively. When detuning Δ_2 has a positive (negative) value, the two dressed states will shift upward (downward) according to the eigenfrequencies expression. These characteristics can also help us to alter the EIG, so we can control the EIG by the intensities and detunings of the \mathbf{E}_2 and \mathbf{E}'_2 beams. Moreover, the nonlinear optical susceptibility $\chi^{(3)}$ can be enhanced when the two-photon resonance condition ($\Delta_1 + \Delta_2 = 0$) is satisfied [27], so we can also control the EIG by altering Δ_1 .

To demonstrate the spatial distribution of the EIG of $\chi^{(3)}$, we show the intensity distribution of the anti-Stokes signal in Fig. 2(b), where the intensity distribution as a function of x and Δ_1 is obtained from the normalized amplitude of $\rho_{20(\text{as})}^{(3)}$. In Fig. 2(b), when scanning Δ_1 while keeping $\Delta_2 = 0$ at $z = 0$, we can see a single peak at the nodes of the dressed-state levels and two peaks at the antinodes of the dressed-state levels. This can be explained by the dressed-state analysis as shown in Fig. 2(a1). The double peaks are the Autler-Townes doublet, which result from the dressing effect of the standing wave. At the nodes, the Rabi frequency of the standing wave is zero due to the destructive interference of the \mathbf{E}_2 and \mathbf{E}'_2 beams, so there is no dressing effect from the standing wave, and then only a single peak can be observed in the intensity distribution of the anti-Stokes signal. At the antinodes, the Rabi frequency has maximum value, so the two dressed-state levels with the largest

separation can be obtained and the Autler-Townes doublet can be observed. Therefore the EIG can be established by the standing wave in the atomic medium, and the EIG structure can be easily controlled by the optical fields.

III. SOTE WITH BIPHOTONS

Since the SPFWM process absorbs two pump photons and produces one Stokes and one anti-Stokes photon simultaneously, the two output photons of the SPFWM process are highly correlated. In the frequency space, they are entangled owing to the frequency PMC $2\omega_1 = \omega_{\text{as}} + \omega_s$. They are also entangled with respect to the wave vector since they satisfy the momentum conservation condition $\mathbf{k}_{s,\rho} + \mathbf{k}_{\text{as},\rho} = 2\mathbf{k}_1$, which implies the spatial correlation of the photon pairs. The wave-vector correlation is of prime interest in second-order Talbot imaging. In this paper, we will discuss how to achieve SOTE by using the two-photon spatial correlation. This SOTE scheme has a ghost imaging configuration [28–30], where the entangled photon pairs serve as the imaging light and the nonmaterial grating can be imaged nonlocally without using any focus lens. Then the second-order two-photon Talbot self-image can be obtained by coincidence count according to Glauber's quantum measurement theory [31]. To study the SOTE resulting from the SPFWM process, let us look at the two-photon joint-detection measurements as shown in Fig. 1(b), where Stokes photons are detected by D_s and anti-Stokes photons by D_{as} . The normalized second-order correlation function in this process can be expressed as

$$g^{(2)} = \frac{\langle E_s^{(-)}(\mathbf{r}_s, t_s) E_{\text{as}}^{(-)}(\mathbf{r}_{\text{as}}, t_{\text{as}}) E_{\text{as}}^{(+)}(\mathbf{r}_{\text{as}}, t_{\text{as}}) E_s^{(+)}(\mathbf{r}_s, t_s) \rangle}{\langle E_s^{(-)}(\mathbf{r}_s, t_s) E_s^{(+)}(\mathbf{r}_s, t_s) \rangle \langle E_{\text{as}}^{(-)}(\mathbf{r}_{\text{as}}, t_{\text{as}}) E_{\text{as}}^{(+)}(\mathbf{r}_{\text{as}}, t_{\text{as}}) \rangle}, \quad (1)$$

where $E_i^{(+)}(\mathbf{r}_i, t_i)$ and $E_i^{(-)}(\mathbf{r}_i, t_i)$ ($i = s$ or as) are the positive- and negative-frequency parts of the electric field evaluated at position \mathbf{r}_i and detection time t_i .

First, we use the differential wave interaction equations to describe the propagation of the Stokes and anti-Stokes photons [32]. According to these equations, the output Stokes and anti-Stokes fields at the surface of the atomic medium can

be obtained as

$$\begin{aligned}\hat{a}_s(L) &= \cosh(\kappa L)\hat{a}_s(0) + \sinh(\kappa L)\hat{a}_{as}^\dagger(0) \\ \hat{a}_{as}^\dagger(L) &= \cosh(\kappa L)\hat{a}_{as}^\dagger(0) + \sinh(\kappa L)\hat{a}_s(0)\end{aligned}\quad (2)$$

Here, we just consider the single angular frequency mode. L is the interaction distance of the wave; κ is the nonlinear coupling coefficient. $\hat{a}_s(L)$ [$\hat{a}_s^+(L)$] and $\hat{a}_{as}(L)$ [$\hat{a}_{as}^+(L)$] are referred to as the annihilation (creation) operators of the output Stokes and anti-Stokes photons, respectively. $\hat{a}_s(0)$ [$\hat{a}_s^+(0)$] and $\hat{a}_{as}(0)$ [$\hat{a}_{as}^+(0)$] represent the annihilation (creation) operators of the input Stokes and anti-Stokes photons, respectively. If there are no seeded fields at the Stokes and anti-Stokes ports, the input fields will be the vacuum fields. The electric fields detected by a photodetector can be described by the electric fields on the output surfaces of the medium using the Green's function, which is the optical transfer function and describes the propagation of each transverse mode,

$$\begin{aligned}E_i^{(+)}(\mathbf{r}_i, t_i) &= E_i^{(+)}(\boldsymbol{\rho}_i, z_i, t_i) \\ &= \sum_{\mathbf{k}_i} E_i g_i(\mathbf{k}_i, \omega_i; \boldsymbol{\rho}_i, z_i) \hat{a}_i(L) e^{-i\omega_i t_i} \quad (i = s, as),\end{aligned}\quad (3)$$

where $E_i = \sqrt{\hbar\omega_i/2\epsilon_0}$, \mathbf{k}_i is the transverse wave vector, and ω_i denotes the frequency of the generated Stokes and anti-Stokes

fields. $g_i(\mathbf{k}_i, \omega_i; \boldsymbol{\rho}_i, z_i)$ is the Green's function and describes the propagation of the mode with angular frequency ω_i and transverse wave vector \mathbf{k}_i from the source to the transverse coordinate $\boldsymbol{\rho}_i$ of the detector D_i , which is at the distance of z_i from the output surface of the atomic medium to the plane of the detector. The Green's function can be written as [31,33,34]

$$\begin{aligned}g_s(\mathbf{k}_s, \omega_s; \boldsymbol{\rho}_s, z_s) &= \frac{-i\omega_s}{2\pi c z_s} e^{i\frac{\omega_s}{c} z_s} \int_{\text{source}} d\boldsymbol{\rho}_{so} T(\boldsymbol{\rho}_{so}) \\ &\quad \times \left\{ e^{-i\mathbf{k}_s \cdot \boldsymbol{\rho}_{so}} e^{i\frac{\omega_s}{2cz_s} |\boldsymbol{\rho}_{so} - \boldsymbol{\rho}_s|^2} \right\}, \\ g_{as}(\mathbf{k}_{as}, \omega_{as}; \boldsymbol{\rho}_{as}, z_{as}) &= \frac{-i\omega_{as}}{2\pi c z_{as}} e^{i\frac{\omega_{as}}{c} z_{as}} \int_{\text{source}} d\boldsymbol{\rho}'_{so} T(\boldsymbol{\rho}'_{so}) \\ &\quad \times \left\{ e^{-i\mathbf{k}_{as} \cdot \boldsymbol{\rho}'_{so}} e^{i\frac{\omega_{as}}{2cz_{as}} |\boldsymbol{\rho}'_{so} - \boldsymbol{\rho}_{as}|^2} \right\},\end{aligned}\quad (4)$$

where $\boldsymbol{\rho}_{so}$ and $\boldsymbol{\rho}'_{so}$ are transverse wave vectors defined on the output plane of the periodic source, $\boldsymbol{\rho}_i$ ($i = s, as$) are the transverse vectors on the plane of the detector, $T(\boldsymbol{\rho}_{so})$ is the transmission function for the EIG induced by standing wave, and c is the speed of light.

According to the definition of the second-order correlation function, the three terms $\langle E_s^{(-)}(\mathbf{r}_s, t_s) E_{as}^{(-)}(\mathbf{r}_{as}, t_{as}) E_{as}^{(+)}(\mathbf{r}_{as}, t_{as}) E_s^{(+)}(\mathbf{r}_s, t_s) \rangle$, $\langle E_s^{(-)}(\mathbf{r}_s, t_s) E_s^{(+)}(\mathbf{r}_s, t_s) \rangle$, and $\langle E_{as}^{(-)}(\mathbf{r}_{as}, t_{as}) E_{as}^{(+)}(\mathbf{r}_{as}, t_{as}) \rangle$ can be calculated as follows:

$$\begin{aligned}&\langle E_s^{(-)}(\mathbf{r}_s, t_s) E_{as}^{(-)}(\mathbf{r}_{as}, t_{as}) E_{as}^{(+)}(\mathbf{r}_{as}, t_{as}) E_s^{(+)}(\mathbf{r}_s, t_s) \rangle \\ &= R_{as}^2 E_{as}^2 E_s^2 |\cosh(\kappa L) \sinh(\kappa L)|^2 \left| \int d\mathbf{k}_{as\rho} \int d\omega_{as} g_s(\mathbf{k}_{s\rho}, \boldsymbol{\rho}_s) g_{as}(\mathbf{k}_{as\rho}, \boldsymbol{\rho}_{as}) e^{-i\omega_{as}\tau} \right|^2 \\ &\quad + R_s E_s^2 |\sinh(\kappa L)|^2 \int d\mathbf{k}_{s\rho} \int d\omega_s |g_s(\mathbf{k}_{s\rho}, \boldsymbol{\rho}_s)|^2 R_{as} E_{as}^2 |\sinh(\kappa L)|^2 \int d\mathbf{k}_{as\rho} \int d\omega_{as} |g_{as}(\mathbf{k}_{as\rho}, \boldsymbol{\rho}_{as})|^2,\end{aligned}\quad (5a)$$

$$\langle E_s^{(-)}(\mathbf{r}_s, t_s) E_s^{(+)}(\mathbf{r}_s, t_s) \rangle = E_s^2 R_s |\sinh(\kappa L)|^2 \int d\mathbf{k}_{s\rho} \int d\omega_s |g_s(\mathbf{k}_{s\rho}, \boldsymbol{\rho}_s)|^2, \quad (5b)$$

$$\langle E_{as}^{(-)}(\mathbf{r}_{as}, t_{as}) E_{as}^{(+)}(\mathbf{r}_{as}, t_{as}) \rangle = E_{as}^2 R_{as} |\sinh(\kappa L)|^2 \int d\mathbf{k}_{as\rho} \int d\omega_{as} |g_{as}(\mathbf{k}_{as\rho}, \boldsymbol{\rho}_{as})|^2, \quad (5c)$$

where $\tau = t_{as} - t_s$ and we have used the approximation

$$\sum_{\mathbf{k}_i} \rightarrow \frac{V}{(2\pi)^3} \int d\mathbf{k}_i = \frac{V}{(2\pi)^3} \int d\mathbf{k}_{i\rho} \int \frac{dk_{iz}}{d\omega_i} d\omega_i = \frac{V}{(2\pi)^3} \int d\mathbf{k}_{i\rho} \int \frac{d\omega_i}{v_i} = R_i \int d\mathbf{k}_{i\rho} \int d\omega_i.$$

Here $R_i = V/[2\pi^3 v_i]$ ($i = s, as$) and v_i is the velocity of the field.

We just consider the wave-vector correlation in our paper, so we assume that the Stokes and anti-Stokes photons have the single angular frequency. Thus $\sum_{\mathbf{k}_i} = R_i \int d\mathbf{k}_{i\rho}$ (R_i is a constant). Therefore the three terms in Eq. (5) can be calculated as

$$\begin{aligned}&\langle E_s^{(-)}(\mathbf{r}_s, t_s) E_{as}^{(-)}(\mathbf{r}_{as}, t_{as}) E_{as}^{(+)}(\mathbf{r}_{as}, t_{as}) E_s^{(+)}(\mathbf{r}_s, t_s) \rangle \\ &= R_{as}^2 E_{as}^2 E_s^2 |\cosh(\kappa L) \sinh(\kappa L)|^2 C_1 + E_s^2 R_s |\sinh(\kappa L)|^2 C_2 E_{as}^2 R_{as} |\sinh(\kappa L)|^2 C_3,\end{aligned}\quad (6a)$$

$$\langle E_s^{(-)}(\mathbf{r}_s, t_s) E_s^{(+)}(\mathbf{r}_s, t_s) \rangle = E_s^2 R_s |\sinh(\kappa L)|^2 C_2, \quad (6b)$$

$$\langle E_{as}^{(-)}(\mathbf{r}_{as}, t_{as}) E_{as}^{(+)}(\mathbf{r}_{as}, t_{as}) \rangle = E_{as}^2 R_{as} |\sinh(\kappa L)|^2 C_3, \quad (6c)$$

where

$$C_1 = \left(\frac{\omega_s}{2\pi c z_s} \frac{\omega_{as}}{2\pi c z_{as}} \right)^2 \left| \int_{\text{source}} d^2 \rho_{so} T^2(\rho_{so}) e^{i \frac{\omega_s}{2c z_s} |\rho_{so} - \rho_s|^2} \times e^{i \frac{\omega_{as}}{2c z_{as}} |\rho_{so} - \rho_{as}|^2} \right|^2, \quad (7a)$$

$$C_2 = \left(\frac{\omega_s}{2\pi c z_s} \right)^2 \int_{\text{source}} d^2 \rho_{so} T^2(\rho_{so}), \quad (7b)$$

$$C_3 = \left(\frac{\omega_{as}}{2\pi c z_{as}} \right)^2 \int_{\text{source}} d^2 \rho_{so} T^2(\rho_{so}). \quad (7c)$$

C_2 and C_3 are constants. C_1 is of basic importance for the biphotonic correlation. In our paper, the periodic source is a one-dimensional spatially periodic EIG. For simplicity, we only discuss one-dimensional EIG, but extension of the analysis to two-dimensional EIG is straightforward. We change vector ρ_{so} into scalar x for one-dimensional EIG, then $T(\rho_{so})$ is replaced by $T(x)$, which is proportional to the amplitude of $\rho_{20}^{(3)}$. The transmission function for a general one-dimensional periodic object can be expressed by a Fourier series, so $T(x)$ can be expanded as $T(x) = \sum_{n=-\infty}^{+\infty} c_n e^{-i(2\pi n x/a_x)}$, where a_x is the spatial period along the x direction and c_n is the coefficient of the n th harmonic. Because any type of periodic object can be assumed for the present analysis, we will not specify the form of c_n . Substituting the Fourier expansion of the $T(x)$ into Eq. (7a) and assuming that $z_s = z_{as} = z$, we can calculate C_1 to be

$$C_1 = \left(\frac{\omega_s}{2\pi c z} \frac{\omega_{as}}{2\pi c z} \right)^2 \left| \sum_{n=-\infty}^{+\infty} c_n^2 e^{-i\pi \frac{a_x^2}{2a_x^2} \lambda z} e^{-i \frac{\pi n}{a_x} (x_s + x_{as})} \right|^2. \quad (8)$$

For simplicity, $R_s = R_{as}$ is assumed, so the biphotonic correlation of Stokes and anti-Stokes fields can be obtained as

$$g^{(2)} = \frac{|\cosh(\kappa L)|^2 C_1}{|\sinh(\kappa L)|^2 C_2 C_3} + 1. \quad (9)$$

From Eq. (9), we can conclude that the biphotonic correlation function is spatially periodic, and the condition for revival patterns of the periodic structure is that the distance z satisfies $z = 4ma_x^2/\lambda$, where $z_{sT} = 4a_x^2/\lambda$ is the second-order Talbot length, and m is an integer. It is noteworthy that the second-order Talbot length is twice the first-order Talbot length.

Next, we will use the biphotonic correlation to investigate SOTE. Let us consider the setup as shown in Fig. 1(b). The Stokes and anti-Stokes photons from the SPFWM process are noncollinear and propagate along two directions. The periodic object is EIG, which creates spatially periodic $\chi^{(3)}$ of the atomic medium for the SPFWM process; so the EIG can be reflected in the entangled photon pairs channels by coincidence count, and the image of the EIG can be observed through the correlation function $g^{(2)}$. The entangled Stokes and anti-Stokes photons are detected by a two-photon detector. The distance between the EIG and the two detectors are all z .

According to Eq. (9), we numerically simulate the second-order correlation pattern by scanning both detectors simultaneously in the same manner along the z direction and the transverse x directions while keeping $\Delta_2 = 0$. The second-order correlation function versus z and x is shown in Fig. 3(a), where the color bar denotes the value of the transverse two-photon correlation, and the longitudinal (transverse) scanning range is $z = 0-50$ cm ($x_s = x_{as} = x = 0-0.6$ mm). We see that a typical Talbot carpet pattern emerges. We can find that the image of the periodic EIG is repeated at integer multiples of Talbot length z_{sT} , and the Talbot length z_{sT} is about 11.5 cm. Here, we are mainly concerned with the control of the Talbot imaging by tuning the optical field. To study the influence of the detuning of Δ_1 to the Talbot imaging, we show the second-order correlation function at different Δ_1 in Figs. 3(a1)–3(a5), where Δ_1 is taken as $-0.8, -0.5, 0, 0.5, 0.8$ MHz, respectively, while $\Delta_2 = 0$ is the same. We can find the contrast of Talbot image (versus x and z) changes with Δ_1 . It increases at first and then decreases with increasing of Δ_1 . Next, we exhibit the transverse profiles of these Talbot carpets at Talbot length distance ($z = 11.5$ cm) in Fig. 3(a6), where the correlation is the highest at the x position corresponding to the nodes of the standing wave, and the correlation is the lowest at the x position corresponding to the antinodes of the standing wave. At $\Delta_1 = 0$, the two-photon resonance condition ($\Delta_1 + \Delta_2 = 0$) is satisfied at the nodes of the standing wave; then the nonlinear optical susceptibility $\chi^{(3)}$ of the SPFWM process is enhanced. At the antinodes of the standing wave with $\Delta_1 = 0$, the two-photon resonance condition ($\Delta_1 + \Delta_2 = 0$) breaks down due to the dressed splitting induced by the standing wave as shown in Fig. 2(a1). Thus the nonlinear optical susceptibility $\chi^{(3)}$ of the SPFWM process is suppressed. Therefore the structure of the EIG can be reflected by the Talbot image. If $\Delta_1 \neq 0$, the two-photon resonance condition cannot be satisfied even at the nodes, where the correlation will decrease. Therefore, the contrast is the highest at $\Delta_1 = 0$, so we can control the contrast by the detuning Δ_1 .

Subsequently, we show that the contrast of the Talbot image can also be controlled by the detuning Δ_2 . The second-order Talbot images versus z , x , and Δ_2 are shown in Fig. 3(b), in which $\Delta_1 = 0$. In Figs. 3(b1)–3(b5), we show the Talbot images in section at different Δ_2 , and the corresponding transverse profiles of the Talbot carpets at Talbot length distance ($z = 11.5$ cm) are shown in Fig. 3(b6). We can see that the contrast of the Talbot image changes with Δ_2 in a different manner. This is because the variation of Δ_2 will make the dressed-state levels shift as shown in Figs. 2(a2) and 2(a3). At the antinodes of the standing wave, when the shift makes the \mathbf{E}_1 field near resonance with the dressed state, the correlation is enhanced. At the nodes, the correlation is not obviously changed due to $|G_{2t}(x)| = 0$, so the contrast can be controlled by Δ_2 , and the contrast is the highest when $\Delta_2 = 0$.

IV. SOTE WITH SPATIALLY CORRELATED TWIN BEAMS

In this part, we demonstrate the SPFWM process when two other strong fields, \mathbf{E}_3 and \mathbf{E}'_3 , are added as shown in Fig. 1(c). Both \mathbf{E}_3 and \mathbf{E}'_3 beams counterpropagate with the \mathbf{E}_1 beam. There is a very small angle between the \mathbf{E}_3 and \mathbf{E}'_3 beams. If the detunings of the \mathbf{E}_3 and \mathbf{E}'_3 beams are not equal,

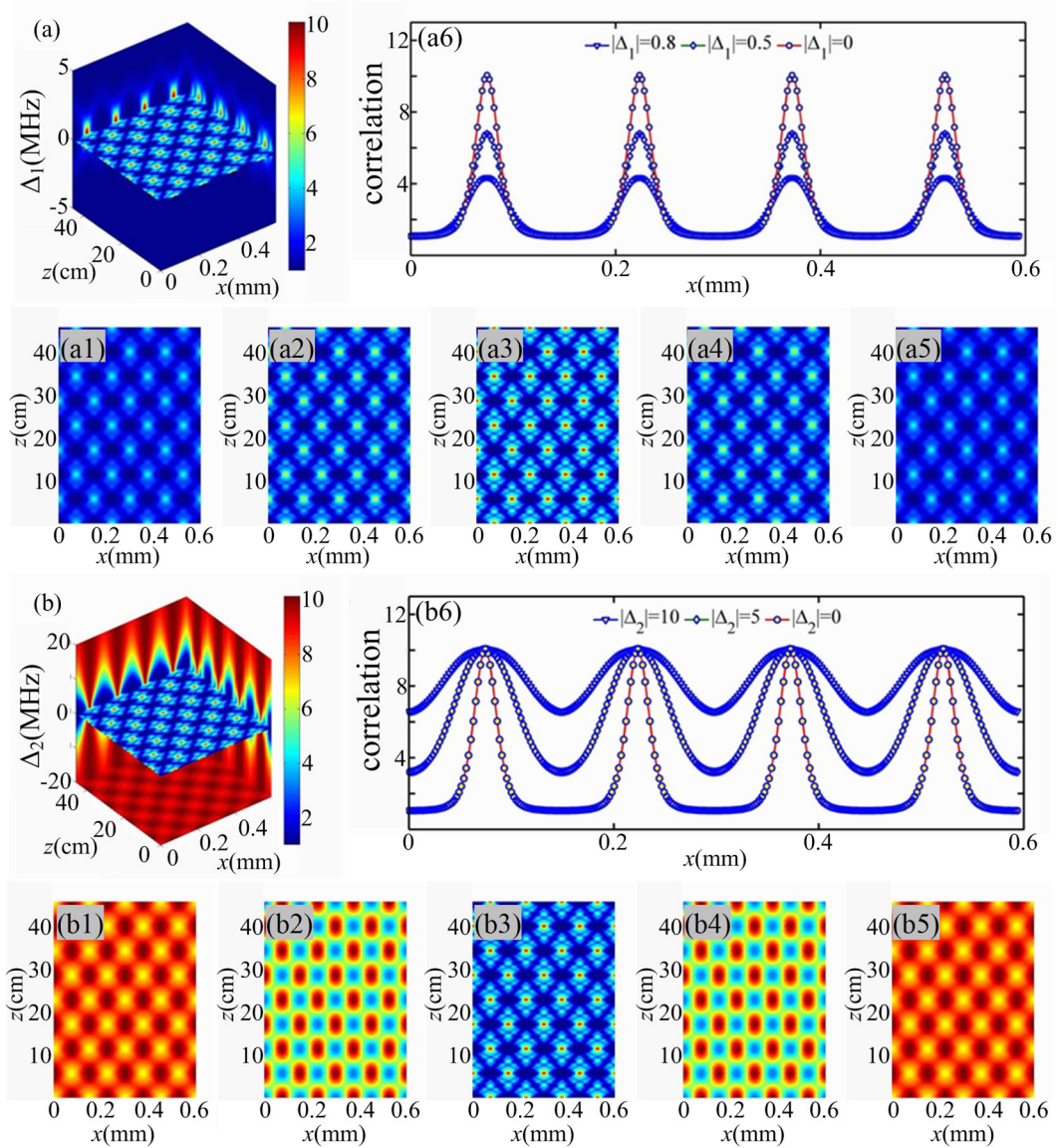


FIG. 3. (Color online) (a) Theoretical Talbot imaging carpets versus Δ_1 , x , and z obtained by scanning both detectors simultaneously through $z = 0-50$ cm along the z direction and through $x = 0-0.6$ mm ($x_s = x_{as} = x$) along the transverse x directions while keeping $\Delta_2 = 0$ (a1–a5) Talbot imaging carpets versus x and z with $\Delta_2 = 0$: $\Delta_1 = -0.8, -0.5, 0, 0.5, 0.8$ MHz from left to right, respectively; (a6) second-order correlation degree versus x at a Talbot length distance ($z = 11.5$ cm) with $\Delta_2 = 0$: $|\Delta_1| = 0$ MHz (top curve), $|\Delta_1| = 0.5$ MHz (middle curve), and $|\Delta_1| = 0.8$ MHz (bottom curve). (b) Theoretical Talbot imaging carpets versus Δ_2 , x , and z obtained by scanning both detectors simultaneously through $z = 0-50$ cm along the z direction and through $x = 0-0.6$ mm ($x_s = x_{as} = x$) along the transverse x directions while keeping $\Delta_1 = 0$: (b1–b5) Talbot imaging carpets versus x and z with $\Delta_1 = 0$: $D_2 = -10, -5, 0, 5, 10$ MHz from left to right, respectively; (b6) second-order correlation degree versus x at a Talbot length distance ($z = 11.5$ cm) with $\Delta_1 = 0$: $|\Delta_2| = 10$ MHz (top curve), $|\Delta_2| = 5$ MHz (middle curve), and $|\Delta_2| = 0$ MHz (bottom curve). The other parameters are chosen: $G_1 = 20$ MHz, $G_2 = G'_2 = 45$ MHz, $\Gamma_{10} = 0.2\Gamma_{20}$, $\Gamma_{30} = 0.1\Gamma_{20}$, $\Gamma_{20} = \Gamma_{21} = 2\pi \times 6$ MHz, $a_x = 150 \mu\text{m}$, and $\lambda_1 = 780.240$ nm.

and the \mathbf{E}'_3 beam relative to the \mathbf{E}_3 beam is detuned by the ground-state splitting of the atomic system, the system will generate a phase-conjugate FWM and two phase-conjugate SWM signals, which satisfy the PMCs $\mathbf{k}_{fw} = \mathbf{k}_1 + \mathbf{k}_3 - \mathbf{k}'_3$ and $\mathbf{k}_{sw} = \mathbf{k}_1 + \mathbf{k}_2(\mathbf{k}'_2) - \mathbf{k}_2(\mathbf{k}'_2) + \mathbf{k}_3 - \mathbf{k}'_3$, respectively. According to the PMCs, we find that the phase-conjugate FWM and SWM signals propagate along the same direction, which is opposite to that of the \mathbf{E}'_3 beam. The frequency of the phase-conjugate FWM and SWM signals are the same as the central frequency of the Stokes signal. If the phase-conjugate

FWM and SWM signal are seeded into the Stokes port as shown in Fig. 1(c), the whole process can be viewed as an optical parametric amplifier, which can generate the spatially correlated twin beams. In this process, the power of the \mathbf{E}_3 and \mathbf{E}'_3 beams is usually strong, so the dressing effect of the \mathbf{E}_3 and \mathbf{E}'_3 fields should also be considered. The dressing effect from the \mathbf{E}_3 and \mathbf{E}'_3 fields is not periodic, because their frequency is different. Generally, the detuning of the \mathbf{E}'_3 beam is much larger than that of the \mathbf{E}_3 beam. Therefore we only consider the dressing effect from the \mathbf{E}_3 field. Then the dressed density

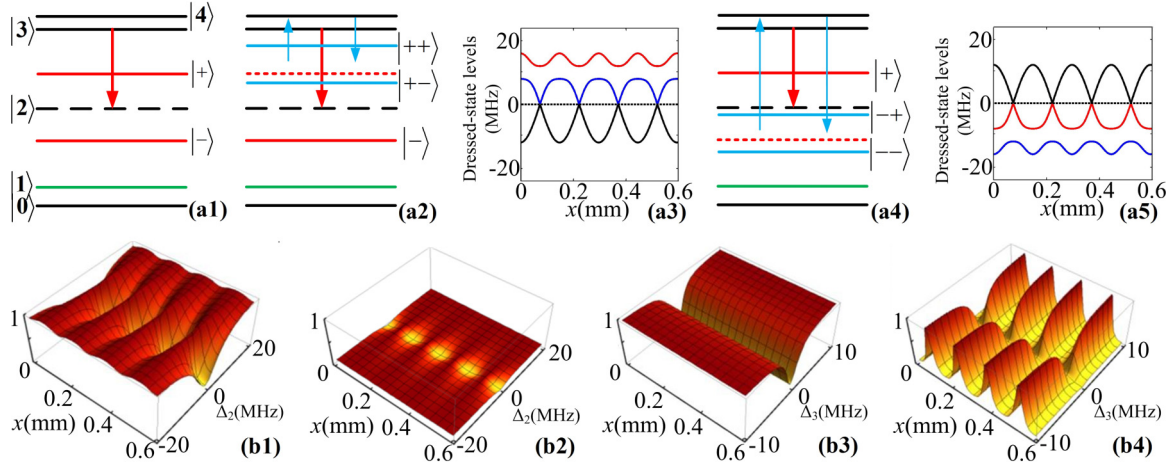


FIG. 4. (Color online) (a1) The primary dressing splitting induced by the standing wave; (a2) the secondary dressing splitting created by the \mathbf{E}_3 field when the \mathbf{E}_3 field is tuned close to the dressed states $|+\rangle$, $|++\rangle$, and $|+-\rangle$, representing secondary dressed states; (a3) doubly-dressed-state levels corresponding to (a2). Parameters are chosen: $G_2 = G'_2 = 6$ MHz, $\Delta_2 = 0$, $G_3 = 4$ MHz, $\Delta_3 = 12$ MHz; (a4) the secondary dressing splitting created by the \mathbf{E}_3 field when the \mathbf{E}_3 field is tuned close to the dressed states $|-\rangle$, $|-\rangle$, and $|--\rangle$, representing secondary dressed states; (a5) doubly-dressed-state levels corresponding to (a4). Parameters are chosen: $G_2 = G'_2 = 6$ MHz, $\Delta_2 = 0$, $G_3 = 4$ MHz, $\Delta_3 = -12$ MHz. (b1,b2) Theoretical simulation of the normalized intensity distribution of the anti-Stokes signal versus x and Δ_2 with primary dressing of standing wave (i.e., \mathbf{E}_3 and \mathbf{E}'_3 beams are turned off) and double dressing (i.e., \mathbf{E}_3 and \mathbf{E}'_3 beams are turned on), respectively, and $\Delta_3 = 0$; (b3,b4) theoretical simulation of the normalized intensity distribution of the anti-Stokes signal versus x and Δ_3 with primary dressing of the \mathbf{E}_3 field (i.e., \mathbf{E}_2 and \mathbf{E}'_2 beams are turned off) and double dressing (i.e., \mathbf{E}_2 and \mathbf{E}'_2 beams are turned on), respectively, and $\Delta_2 = 0$. Other parameters are $G_1 = 3.5$ MHz, $G_2 = G'_2 = 6$ MHz, $G_3 = 4$ MHz, $\Delta_1 = 0$, $\Gamma_{10} = 0.2\Gamma_{20}$, $\Gamma_{30} = \Gamma_{40} = 0.1\Gamma_{20}$, $\Gamma_{20} = \Gamma_{21} = 2\pi \times 6$ MHz, and $a_x = 150 \mu\text{m}$.

matrix element for the \mathbf{E}_{as} signal can be written as $\rho_{20(\text{as})}^{(3)} = -iG_s^*G_1^2/\{[d_{20}+|G_{2r}(x)|^2/d_{30} + G_3^2/d_{40}]d_{10}d'_{20}\}$ via the corresponding Liouville pathway: $\rho_{00}^{(0)} \xrightarrow{\omega_1} \rho_{G_2(x)\pm G_3\pm 0}^{(1)} \xrightarrow{\omega_s} \rho_{10}^{(2)} \xrightarrow{\omega_1} \rho_{G_2(x)\pm G_3\pm 0(\text{as})}^{(3)}$, where $d_{40} = \Gamma_{40} + i(\Delta_1 + \Delta_3)$. Because the induced periodic $\chi^{(3)}$ in atomic medium is related to $\rho_{20(\text{as})}^{(3)}$, the interference pattern of the EIG field and then the Talbot self-imaging can be controlled by the \mathbf{E}_3 field.

Next, the spatially correlated twin beams are applied to achieve Talbot effects. As mentioned above, if \mathbf{E}_3 and \mathbf{E}'_3 beams are open, the generated phase-conjugate FWM and SWM signals will act as a seed. Then the SPFWM

process will be replaced by an optical parametric amplification (OPA) process and the output fields are correlated twin beams. It has been confirmed that the correlated twin beams have multiple spatial modes [35]. This character makes this source of interest for optical imaging processes. Moreover, the intensities of the generated \mathbf{E}_s and \mathbf{E}_{as} fields are stronger than that obtained from the SPFWM process, so the measurement would be performed more easily.

Similar to the biphotonic correlation function, we calculate $\langle E_s^{(-)}(\mathbf{r}_s, t_s) E_{\text{as}}^{(-)}(\mathbf{r}_{\text{as}}, t_{\text{as}}) E_{\text{as}}^{(+)}(\mathbf{r}_{\text{as}}, t_{\text{as}}) E_s^{(+)}(\mathbf{r}_s, t_s) \rangle$, $\langle E_s^{(-)}(\mathbf{r}_s, t_s) E_s^{(+)}(\mathbf{r}_s, t_s) \rangle$, and $\langle E_{\text{as}}^{(-)}(\mathbf{r}_{\text{as}}, t_{\text{as}}) E_{\text{as}}^{(+)}(\mathbf{r}_{\text{as}}, t_{\text{as}}) \rangle$ with injection as follows:

$$\begin{aligned} \langle E_s^{(-)}(\mathbf{r}_s, t_s) E_{\text{as}}^{(-)}(\mathbf{r}_{\text{as}}, t_{\text{as}}) E_{\text{as}}^{(+)}(\mathbf{r}_{\text{as}}, t_{\text{as}}) E_s^{(+)}(\mathbf{r}_s, t_s) \rangle &= \langle 0, \alpha | E_s^{(-)}(\mathbf{r}_s, t_s) E_{\text{as}}^{(-)}(\mathbf{r}_{\text{as}}, t_{\text{as}}) E_{\text{as}}^{(+)}(\mathbf{r}_{\text{as}}, t_{\text{as}}) E_s^{(+)}(\mathbf{r}_s, t_s) | \alpha, 0 \rangle \\ &= E_{\text{as}}^2 E_s^2 |\cosh(\kappa L) \sinh(\kappa L)|^2 (R_{\text{as}}^2 + R_s^2 |\alpha|^2) C_1 + R_s E_s^2 |\sinh(\kappa L)|^2 (|\alpha|^2 + 1) C_2 R_{\text{as}} E_{\text{as}}^2 |\sinh(\kappa L)|^2 C_3, \end{aligned} \quad (10a)$$

$$\langle E_s^{(-)}(\mathbf{r}_s, t_s) E_s^{(+)}(\mathbf{r}_s, t_s) \rangle = R_s E_s^2 [|\cosh(\kappa L)|^2 |\alpha|^2 + |\sinh(\kappa L)|^2] C_2, \quad (10b)$$

$$\langle E_{\text{as}}^{(-)}(\mathbf{r}_{\text{as}}, t_{\text{as}}) E_{\text{as}}^{(+)}(\mathbf{r}_{\text{as}}, t_{\text{as}}) \rangle = R_{\text{as}} E_{\text{as}}^2 (|\alpha|^2 + 1) |\sinh(\kappa L)|^2 C_3. \quad (10c)$$

Thus, the intensity correlation function can be obtained as

$$g^{(2)} = \frac{|\cosh(\kappa L)|^2}{[|\cosh(\kappa L)|^2 |\alpha|^2 + |\sinh(\kappa L)|^2]} \frac{C_1}{C_2 C_3} + \frac{|\sinh(\kappa L)|^2}{[|\cosh(\kappa L)|^2 |\alpha|^2 + |\sinh(\kappa L)|^2]}, \quad (11)$$

where $\langle \hat{a}_{\text{as}}^\dagger(0) \hat{a}_{\text{as}}(0) \rangle = |\alpha|^2$, which refers to the injection intensity of FWM and SWM signals. The expressions for C_i

($i = 1, 2, 3$) have been given in Eq. (7). We can find that the correlation function is spatially periodic due to C_1 , and the

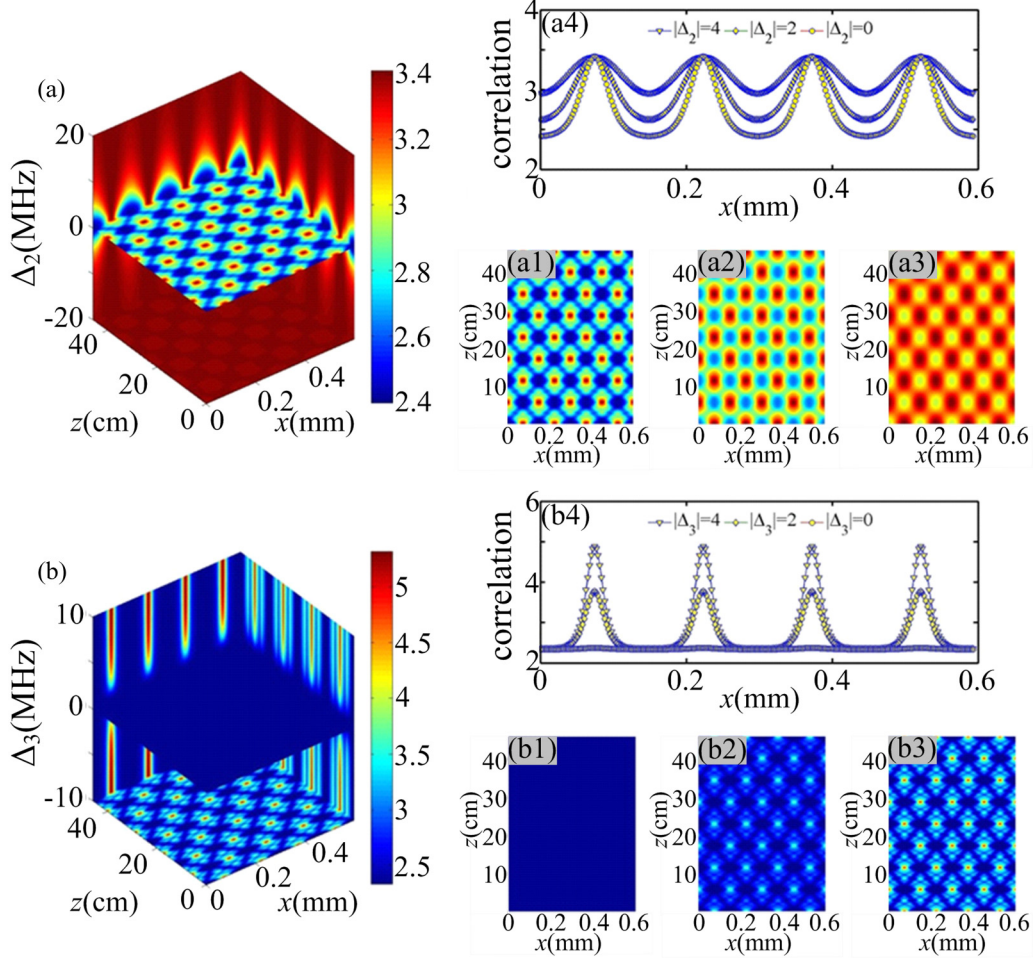


FIG. 5. (Color online) (a) Theoretical Talbot imaging carpets versus Δ_2 , x , and z obtained by scanning both detectors simultaneously through $z = 0\text{--}50$ cm along the z direction and through $x = 0\text{--}0.6$ mm along the transverse x directions in the OPA process while keeping $\Delta_1 = 0$ and $\Delta_3 = 1.5$ MHz : (a1–a3) Talbot imaging carpets with $|\Delta_2| = 0, 2, 4$ MHz, respectively; (a4) second-order correlation degree versus x at a Talbot length distance ($z = 11.5$ cm): $|\Delta_2| = 4$ MHz (top curve), $|\Delta_2| = 2$ MHz (middle curve), and $|\Delta_2| = 0$ MHz (bottom curve). (b) Theoretical Talbot imaging carpets versus Δ_3 , x , and z obtained by scanning both detectors simultaneously through $z = 0\text{--}50$ cm along the z direction and through $x = 0\text{--}0.6$ mm along the transverse x directions in the OPA process while keeping $\Delta_1 = \Delta_2 = 0$: (b1–b3) Talbot imaging carpets with $|\Delta_3| = 0, 2, 4$ MHz, respectively; (b4) second-order correlation degree versus x at a Talbot length distance ($z = 11.5$ cm): $|\Delta_3| = 4$ MHz (top curve), $|\Delta_3| = 2$ MHz (middle curve), and $|\Delta_3| = 0$ MHz (bottom curve). The other parameters are chosen: $G_1 = 20$ MHz, $G_2 = G'_2 = 45$ MHz, $G_3 = G'_3 = 25$ MHz, $\Gamma_{10} = 0.2\Gamma_{20}$, $\Gamma_{30} = \Gamma_{40} = 0.1\Gamma_{20}$, $\Gamma_{20} = \Gamma_{21} = 2\pi \times 6$ MHz, $a_x = 150$ μm , and $\lambda_1 = 780.240$ nm.

periodic structure can be revived at the second-order Talbot length. Moreover, the second-order correlation and contrast decrease when there is injection in the Stokes spot. This is because the injection will enhance the number of the entangled photon pairs at the cost of the spatial correlation. When there is no injection [i.e., $\langle \hat{a}_{\text{as}}^\dagger(0)\hat{a}_{\text{as}}(0) \rangle = 0$], the results return to the case for the biphotonic correlation in Eq. (9).

Now, let us show the EIG structure and investigate how to control it in the OPA process. From the above analysis, we know the dressing effect of the \mathbf{E}_3 field should be considered in the OPA process. Therefore the doubly-dressed-state analysis

will be used. We may consider the coupled atom-field system, which consists of states $|2\rangle$, $|3\rangle$, $|4\rangle$, the standing wave, and the \mathbf{E}_3 field, by two steps. First, the interaction of the standing wave and atom with states $|2\rangle$ and $|3\rangle$ creates primary dressed states $|\pm\rangle$ as shown in Fig. 4(a1). Next, consider secondary dressed states created by the \mathbf{E}_3 field. When the \mathbf{E}_3 field is tuned close to the dressed states $|+\rangle$ (or $|-\rangle$) as shown in Fig. 4(a2) [or Fig. 4(a4)], we can consider that the \mathbf{E}_3 field only couples the dressed state $|+\rangle$ (or $|-\rangle$) to state $|4\rangle$ and leaves the other dressed state $|-\rangle$ (or $|+\rangle$) unperturbed. Then the eigenfrequencies for three dressed states can be given by

$$\lambda_{G_{2l}(x)+G_3\pm} = \frac{\Delta_2 + \sqrt{\Delta_2^2 + 4|G_{2l}(x)|^2}}{2} + \frac{\Delta_{3\pm} \pm \sqrt{\Delta_{3\pm}^2 + 4|G_3|^2}}{2}, \quad \text{and} \quad \lambda_{G_{2l}(x)-} = \frac{\Delta_2 - \sqrt{\Delta_2^2 + 4|G_{2l}(x)|^2}}{2}, \quad (12a)$$

or

$$\lambda_{G_{2t}(x)+} = \frac{\Delta_2 + \sqrt{\Delta_2^2 + 4|G_{2t}(x)|^2}}{2} \quad \text{and} \quad \lambda_{G_{2t}(x)-G_3\pm} = \frac{\Delta_2 - \sqrt{\Delta_2^2 + 4|G_{2t}(x)|^2}}{2} + \frac{\Delta_{3-} \pm \sqrt{\Delta_{3-}^2 + 4|G_3|^2}}{2}, \quad (12b)$$

where $\Delta_{3+} = \Delta_3 - [\Delta_2 + \sqrt{\Delta_2^2 + 4|G_{2t}(x)|^2}]/2$ and $\Delta_{3-} = \Delta_3 - [\Delta_2 - \sqrt{\Delta_2^2 + 4|G_{2t}(x)|^2}]/2$, respectively. According to Eq. (12), we show the dressed-state levels in Figs. 4(a3) and 4(a5), which correspond to the cases in Figs. 4(a2) and 4(a4), respectively. Therefore we can control the structure of the EIG by the \mathbf{E}_3 beam besides the \mathbf{E}_2 and \mathbf{E}'_2 beams in the OPA process. To demonstrate the $\chi^{(3)}$ EIG structure, we show the intensity distribution of the anti-Stokes signal in Figs. 4(b1)–4(b4), where $\Delta_1 = 0$ is set. When the \mathbf{E}_3 and \mathbf{E}'_3 beams are turned off, the normalized intensity distribution of the anti-Stokes signal versus x and Δ_2 is shown in Fig. 4(b1), where the spatially periodic suppression of the intensity can be observed. The results are the same as the case for the biphotonic process. The spatially periodic suppression results from the dressing of the standing wave. At the antinodes, the intensity of the anti-Stokes signal will be suppressed, and the intensity will not be affected by the standing wave at the nodes. The period of the intensity suppression reflects in the period of the EIG. When the \mathbf{E}_3 and \mathbf{E}'_3 beams are open and $\Delta_3 = 0$ is set, the corresponding intensity of the anti-Stokes signal is shown in Fig. 4(b2), where the dressing effect of the \mathbf{E}_3 field is included. We can see the intensity of the anti-Stokes signal in Fig. 4(b2) is greatly suppressed compared with that in Fig. 4(b1). The suppression proves that the nonlinear optical susceptibility $\chi^{(3)}$ can be altered by the \mathbf{E}_3 field. We also show the normalized intensity distribution of the anti-Stokes signal versus x and Δ_3 in Figs. 4(b3) and 4(b4), where the results are obtained with \mathbf{E}_2 and \mathbf{E}'_2 turned off and on, respectively. In Fig. 4(b3), the intensity of the anti-Stokes signal can be suppressed at $\Delta_3 = 0$, because of the dressed splitting of the energy level induced by the \mathbf{E}_3 field. If the \mathbf{E}_2 and \mathbf{E}'_2 beams are turned on, the dressing effect from the standing wave is reflected in the spatially periodical anti-Stokes signal.

Subsequently, we show the Talbot images by using the spatially correlated twin beams. According to Eq. (11), we show the numerically simulated second-order correlation pattern in Fig. 5 by scanning both detectors simultaneously in the same manner along the z direction and the transverse x directions. The longitudinal and transverse scanning range are $z = 0$ –50 cm and $x = 0$ –0.6 mm, respectively. We find the image of the periodic structure is repeated at integer multiples of the second-order Talbot length z_{sT} in Figs. 5(a1)–5(a3), where $\Delta_1 = 0$ MHz and $\Delta_3 = 1.5$ MHz. It is also observed that the contrast of the image changes with Δ_2 . The variance with Δ_2 is similar to that in Fig. 3(b). However, the spatial correlation and correlation contrast in Fig. 5(a4) are smaller than that in Fig. 3(b6) because of the injection of the FWM and SWM signals. Moreover, we study the influence of the detuning of Δ_3 to the Talbot imaging and show the second-order correlation function at different Δ_3 in Figs. 5(b1)–5(b3),

where $|\Delta_3| = 0, 2, 4$ MHz, respectively, while $\Delta_1 = \Delta_2 = 0$ is the same. We can find the contrast of the image is nearly zero when $|\Delta_3| = 0$. This is in accordance with the EIG structure with $\Delta_3 = 0$ as shown in Fig. 4(b2), where the two-photon resonance condition ($\Delta_1 + \Delta_2 = 0$) at the nodes of the standing wave breaks down due to the dressed splitting induced by the \mathbf{E}_3 field. Therefore the correlation at the nodes will greatly decrease. When the \mathbf{E}_3 field is tuned away from the resonance, the dressing effect gradually decreases, and then the correlation will increase at the nodes. At the antinodes, the correlation is not affected because the detuning Δ_3 is much smaller than the Rabi frequency of the standing wave.

V. CONCLUSION

In summary, we theoretically study SOTE by the FWM process in the cold atomic medium. The nonlinear optical susceptibility $\chi^{(3)}$ grating induced by a standing wave can be periodically modulated by the dressing effect. The generated signals are weak without the injection in the SPFWM process, and we can use the biphotonic correlation to achieve the Talbot effect. When the phase-conjugate FWM and SWM signals are injected into the SPFWM process, the generated signals are spatially correlated twin beams with stronger intensities, so we can also use them to achieve the Talbot effect. We demonstrate that the nonmaterial grating can be imaged nonlocally, and the image contrast can be controlled simply by adjusting the frequency detuning of the optical fields participating in the process. Moreover, the SOTE achieved by the spatially correlated twin beams may provide an easier scheme to perform the second-order Talbot imaging. Therefore the results may find potential applications in image processing, optical metrology, and spectrometry. Additionally, the entangled photon pairs generated from the SPFWM process have narrow bandwidth, so the SOTE achieved by it may have application in long-distance communications and image transmitting.

ACKNOWLEDGMENTS

This work was supported by the National Nature Science Foundation of China (Grant No. 61205112) and the Research Fund for the Doctoral Program of Higher Education of China (Grant No. 20110201120005). The National Nature Science Foundation of China (Grants No. 11104214, No. 61108017, No. 11104216, and No. 61308015) and Key Scientific and Technological Innovation Team of Shaanxi Province (Grant No. 2014KCT-10) are also acknowledged.

- [1] H. F. Talbot, *Philos. Mag.* **9**, 401 (1836).
- [2] L. Rayleigh, *Philos. Mag.* **11**, 196 (1881).
- [3] R. Iwanow, D. A. May-Arrioja, D. N. Christodoulides, G. I. Stegeman, Y. Min, and W. Sohler, *Phys. Rev. Lett.* **95**, 053902 (2005).
- [4] Y. Wang, K. Zhou, X. Zhang, K. Yang, Y. Wang, Y. Song, and S. Liu, *Opt. Lett.* **35**, 685 (2010).
- [5] M. R. Dennis, N. I. Zheludev, and F. J. G. de Abajo, *Opt. Express* **15**, 9692 (2007).
- [6] A. A. Maradudin and T. A. Leskova, *New J. Phys.* **11**, 033004 (2009).
- [7] L. Deng, E. W. Hagley, J. Denschlag, J. E. Simsarian, M. Edwards, C. W. Clark, K. Helmerson, S. L. Rolston, and W. D. Phillips, *Phys. Rev. Lett.* **83**, 5407 (1999).
- [8] S. J. Wu, E. Su, and M. Prentiss, *Phys. Rev. Lett.* **99**, 173201 (2007).
- [9] Y. Zhang, J. Wen, S. N. Zhu, and M. Xiao, *Phys. Rev. Lett.* **104**, 183901 (2010).
- [10] J. Wen, Y. Zhang, S. N. Zhu, and M. Xiao, *J. Opt. Soc. Am. B* **28**, 275 (2011).
- [11] U. Bortolozzo, S. Residori, and J. P. Huignard, *Opt. Lett.* **31**, 2166 (2006).
- [12] Y. Q. Zhang, M. R. Belic, H. B. Zheng, H. X. Chen, C. B. Li, J. P. Song, and Y. P. Zhang, *Phys. Rev. E* **89**, 032902 (2014).
- [13] X. B. Song, J. Xiong, X. Zhang, and K. Wang, *Phys. Rev. A* **82**, 033823 (2010).
- [14] K. H. Luo, X. H. Chen, Q. Liu, and L. A. Wu, *Phys. Rev. A* **82**, 033803 (2010).
- [15] K. H. Luo, J. M. Wen, X. H. Chen, Q. Liu, M. Xiao, and L. A. Wu, *Phys. Rev. A* **80**, 043820 (2009); **83**, 029902(E) (2011).
- [16] C. H. Raymond Ooi and B. L. Lan, *Phys. Rev. A* **81**, 063832 (2010).
- [17] V. Torres-Company, J. Lancis, H. Lajunen, and A. T. Friberg, *Phys. Rev. A* **84**, 033830 (2011).
- [18] X. B. Song, H. B. Wang, J. Xiong, K. Wang, X. Zhang, K. H. Luo, and L. A. Wu, *Phys. Rev. Lett.* **107**, 033902 (2011).
- [19] A. N. Boto, P. Kok, D. S. Abrams, S. L. Braunstein, C. P. Williams, and J. P. Dowling, *Phys. Rev. Lett.* **85**, 2733 (2000).
- [20] M. D'Angelo, M. V. Chekhova, and Y. H. Shih, *Phys. Rev. Lett.* **87**, 013602 (2001).
- [21] J. M. Wen, S. Du, H. Chen, and M. Xiao, *Appl. Phys. Lett.* **98**, 081108 (2011).
- [22] Y. Q. Zhang, X. Yao, C. Z. Yuan, P. Y. Li, J. M. Yuan, W. K. Feng, S. Q. Jia, and Y. P. Zhang, *IEEE Photon. J.* **4**, 2057 (2012).
- [23] Y. P. Zhang, A. W. Brown, and M. Xiao, *Phys. Rev. Lett.* **99**, 123603 (2007).
- [24] Y. Zhang, U. Khadka, B. Anderson, and M. Xiao, *Phys. Rev. Lett.* **102**, 013601 (2009).
- [25] J. Wen, Y. Zhang, and M. Xiao, *Adv. Opt. Photon.* **5**, 83 (2013).
- [26] M. Yan, E. G. Rickey, and Y. F. Zhu, *Phys. Rev. A* **64**, 013412 (2001).
- [27] M. Fleischhauer, A. Imamoglu, and J. P. Marangos, *Rev. Mod. Phys.* **77**, 633 (2005).
- [28] R. S. Bennink, S. J. Bentley, and R. W. Boyd, *Phys. Rev. Lett.* **89**, 113601 (2002).
- [29] A. Gatti, E. Brambilla, M. Bache, and L. A. Lugiato, *Phys. Rev. Lett.* **93**, 093602 (2004).
- [30] D. V. Strekalov, A. V. Sergienko, D. N. Klyshko, and Y. H. Shih, *Phys. Rev. Lett.* **74**, 3600 (1995).
- [31] J. W. Goodman, *Introduction to Fourier Optics* (McGraw-Hill, New York, 1968).
- [32] K. Bencheikh, E. Huntzinger, and J. A. Levenson, *J. Opt. Soc. Am. B* **12**, 847 (1995).
- [33] M. H. Rubin, *Phys. Rev. A* **54**, 5349 (1996).
- [34] J. M. Wen, P. Xu, M. H. Rubin, and Y. H. Shih, *Phys. Rev. A* **76**, 023828 (2007).
- [35] N. Corzo, A. M. Marino, K. M. Jones, and P. D. Lett, *Opt. Express* **19**, 21358 (2011).